This is the accepted manuscript of the article, which has been published in 2019 41st Annual International Conference of the IEEE Engineering in Medicine and Biology Society (EMBC 2019). Annual International Conference of the IEEE Engineering in Medicine and Biology Society (EMBC). IEEE.
ISBN 978-1-5386-1311-5. ISSN 1557-170X.
https://doi.org/10.1109/EMBC.2019.8857017

Augmenting Soft Tissue Contrast Using Edge-Enhancing Phase-Imaging Techniques in X-Ray Microtomography

A. Reunamo[1], M. Hannula[1], J. Hyttinen[1]

***Abstract*— Conventional X-ray imaging is based on the attenuation of X-rays and the technique provides sufficient contrast when the difference between attenuation coefficients of neighboring structures is sufficient. A promising imaging possibility on a μCT is the use of phase information of an X-ray beam to generate an image of the sample. This is known as phase-contrast imaging. Propagation-based phase imaging sets the least amount of requirements on the imaging setup - lateral coherence for the X-ray source and a movable detector and source. The Zeiss Xradia MicroXCT-400 at our laboratory provides this possibility. Therefore, the phase-contrast imaging protocol, which provides an edge-enhancement effect, on the μCT device was optimized using thin polylactic acid fibers in order to enhance the visibility of low density samples. The optimization consisted of source and detector distance variation measurements. To demonstrate the contrast enhancement results, the optimization was applied to two types of collagen samples embedded in air, ethanol, and water.**

The results showed enhanced contrast for the edge-enhanced phase-contrast images compared to absorption images. Most importantly, the results indicated that the source does not need to placed at the negative limit to obtain useful phase information. Additionally, the visibility increases with increasing sample-to-detector distance. Finally, significantly enhanced contrast was obtained for the collagen sample embedded in water using phase-imaging techniques. The technique is limited due to the focal spot size and voltage of the X-ray source. The phase-imaging technique has the possibility to enhance contrast of low density samples and to reveal structures that cannot be seen using other imaging techniques.

I. INTRODUCTION

Micro-computed tomography or X-ray microtomography (CT) provides a powerful tool for visualization of internal and 3D structures of biological specimens [1], [2], biomaterials [3], [4], and various industrial applications [5], [6]. Conventional X-ray microtomography relies on the attenuation of the X-rays in the sample, which is used to generate an attenuation map of the sample. Sufficient contrast in the resulting images is achieved when the attenuation coefficients of the constituents of the sample differ adequately or staining is used to enhance contrast.[7] Due to this, many structures of soft tissues and various biomaterials are unrecognizable as the attenuation coefficients of neighboring structures are close to each other [8].

The utilization of phase information of an X-ray wavefront to generate contrast has provided a method for imaging low density samples and the technique is called phase-contrast imaging. The refraction of X-rays, far from absorption edges, in a sample can be described by a complex index of refraction

$$n = 1 - \delta + i\beta, \tag{1}$$

where n is the refractive index, δ is the real part of the refractive index, and β is the complex part of the refractive index. The real part of the refractive index is related to the phase shift of the wave ϕ by

$$\phi = \frac{2\pi}{\lambda} \int \delta(l) dl, \tag{2}$$

where λ is the wavelength and the integral is over the path, which the ray has traveled through. As the direct measurement of the induced phase shift is difficult in practice, various setups have been developed for this purpose. These setups differ in their requirements for the system and X-ray source, feasibility, as well as the quantity to be measured. [9], [10]

Propagation-based phase imaging (PBI) was developed by A. Snigirev in 1995 on a synchrotron source [11] and has been since shown to be applicable on conventional polychromatic X-ray sources [8], [12]. The technique is based on the Fresnel diffraction phenomenon resulting in the formation of a holographic image [13]. When the X-ray wavefront comes in contact with the sample, a portion of the incident photons refract due to the differences in refractive indices. The hologram is formed as the refracted photons interfere at some distance from the sample. [9], [10]

PBI sets the least amount of requirements for the imaging setup as it does not require any additional optical devices and requires only spatial coherence from the X-ray source. Additionally, an increase in the sample-to-detector distance compared to absorption imaging is required for phase contrast to be visible. The spatial coherence length determines the amount of phase contrast visible and is given by

$$l_{coh} = \frac{\lambda R_1}{s}, \tag{3}$$

where R_1 is the source-to-sample distance and s is the focal spot size. [9] Consequently, increasing R_1 or decreasing the X-ray energy will result in better phase contrast. The reconstruction of the tomographic image on a laboratory CT is typically done using only the intensity profile of the hologram and a standard reconstruction algorithm. As phase changes typically occur at boundaries, PBI enhance the boundaries of the sample [9]. This is referred to as the edge-enhancement effect. As the manufacturer only states approximate directions for the use of edge-enhancing phase imaging, the purpose of this study was to optimize the phase imaging protocol on the Zeiss Xradia MicroXCT-400 (Zeiss, Pleasanton, CA, USA) by analyzing projection

[1] Tampere University, Faculty of Medicine and Health Technology, Tampere Finland

images obtained with different source-to-sample and sample-to-detector distances. In this study, the images with edge-enhancement are referred to as edge-enhanced phase images even though they also contain absorption information.

II. MATERIALS AND METHODS

The optimization of the edge-enhancing phase imaging protocol on the Zeiss Xradia MicroXCT-400 consisted of the optimization of two variables - source distance and detector distance. Power output and voltage were also included in the optimization [14] but were not presented in this study. Medical grade polylactic acid (PLA) fibers with cross-section lengths of 44, 46, 56, 70, 80, 89, and 107 m were chosen for the optimization process. The fibers had been previously manufactured by a process called melt spinning explained in [15]. The measurements were conducted by placing a PLA fiber in a 1ml syringe and immersing it in ethanol. The syringe was then clamped on a sample holder, which fits the sample stage in the CT.

The source optimization measurements were conducted first for all PLA fibers of different cross-section lengths. For the measurements the detector was set at 70 mm and the source was placed at 370, 300, 230, 160, 90 mm. At each position a projection image was taken after which it was corrected with a reference image taken with the same imaging parameters but without the sample in the field-of-view (FOV). A reference corrected conventional absorption image was also acquired with the source at 40 mm and detector at 10 mm. All projection images were acquired with a voltage of 40 kV and power of 10 W and the exposure time was adjusted so that the photon counts in the middle of the FOV were over 5000. No x-ray filters were used and the pixel size of the projection images ranged from 3.01 μm to 5.97 μm. A magnification of 4x was used for all images and tomographies in addition to the geometric magnification, which depends on the locations of the source and detector.

Image analysis was performed on all projection images, including the conventional absorption image, in the image processing software Fiji [16] once the source distance measurements were conducted. In Fiji, a rectangular selection with a height of 100 pixels was cropped from the images. The width of the selection varied approximately from 60-100 pixels as the fibers were of different sizes. Fiji's Plot Profile -tool was used to generate an intensity profile where the pixel intensities were averaged in the vertical direction resulting in an average pixel intensity plot. These plots were saved as .csv files, which were then imported into MATLAB (MathWorks, Natick, MA, USA) where they were further analyzed. The fiber visibility was analyzed by calculating the percentage decrease between the highest and lowest intensity at the fiber ethanol interface. After the visibilities for one source and detector distance pair was obtained for all fiber sizes, an average of the fiber visibility, called mean percentage difference, was calculated.

After the visibility analysis was performed for the source variation measurements, three source distances (160, 230, and 300 mm) were chosen for further detector distance

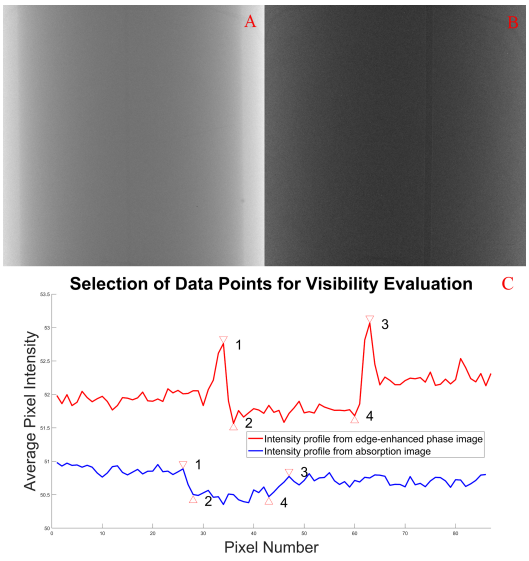

Fig. 1. An absorption image of a 107 m PLA fiber immersed in ethanol in A, a phase image of the same fiber in B, and a depiction of the average intensity profile obtained from an edge-enhanced phase image (in red) and an absorption image (in blue) in C where the peaks represent the fiber edges. A rectangular selection with height of 100 pixels was used to generate the intensity profile. The upside down triangles are the points used in the fiber visibility analysis.

variation measurements. Only three distances were chosen for further analysis as the detector distance range is vast. The same imaging setup was implemented for the measurements. For each source distance the detector distance was varied. The detector distances for which a projection image was acquired were 40, 50, 60, 70, 80, 90, 120, and 200 mm. The imaging parameters were adjusted as previously described and all images were reference corrected. The same fiber visibility analysis was performed on all images. Additionally, contrast-to-noise ratios (CNR) were calculated for all projection images acquired of the 107 m PLA fiber as others were too thin for analysis. CNRs were calculated using $\text{CNR} = \frac{I_\text{O} - I_\text{B}}{STD_\text{B}}$, where I_O and I_B are the mean object and background intensities, respectively and STD_B is the standard deviation of the background. The mean intensities were calculated from a rectangular selection with a height of 100 pixels and width of 14 pixels. The small width was chosen so the rectangular selection would fit inside fiber in all images.

The final aspect of the study was to test the optimized imaging protocol on a sample known to have poor absorption contrast. Pure type I collagen and type I collagen with PLA were chosen as samples, as they were known from previous experiments to have low absorption contrast [3]. Both types of collagen samples had been previously prepared by a technique described in [17]. The collagen samples were stacked on top of each other in a syringe, which was clamped on a sample holder. For the first imaging sequence, air was used as a medium after which the samples were immersed in ethanol and for the last imaging sequence, the samples were embedded in water. The samples were

changed between each acquisition. Tomographic acquisitions were obtained with the source at 230 mm and the detector at 90 mm for all three setups with a voltage of 40 kV and 10 W power. These parameters were chosen due to the fact that CNR calculations were performed after the tomographic acquisitions. Conventional tomographies were also acquired for reference and the exposure time for all tomographies were adjusted as previously described. The voxel size for the tomographies ranged from 4.87 μm to 5.53 μm and the reconstruction algorithm used was a Feldkemp standard filtered back projection algorithm. Visualization of the tomographic datasets was performed on the Avizo 9.5 Software (Thermo Fisher Scientific, Waltham, MA, USA).

III. RESULTS

The results of the fiber visibility analysis and exposure times for the source and detector variation measurements are depicted in fig:allcnrvisi along with the CNR calculations. The graphs are separated to maintain a clear appearance. The visualizations of the cross-sectional slices of the tomographies obtained from the collagen samples in air, ethanol, and water are depicted in fig:colallrey.

From upper left corner of fig:allcnrvisi, it can be seen that the best visibility of the PLA fiber is achieved with a source distance of 230 mm when the detector is at 70 mm. Also visible is the significant increase in exposure time as the source-to-sample distance increases as well as the increase in fiber visibility as the source distance is increased from a typical absorption imaging setup. Evident from the upper right graph in fig:allcnrvisi, increasing the detector distance results in the increase in fiber visibility. As with increasing source-to-sample distance, increasing the sample-to-detector distance also increases the exposure time.

From the lower left graph in fig:allcnrvisi, it can be seen that the CNR increases significantly from the absorption mode to the phase mode imaging, drops after source distance of 160 mm and then stays fairly constant. Results from the CNR analysis on the detector variation are displayed in the lower right graph in fig:allcnrvisi. For source distance of 160 mm, the CNR decreases with increasing detector distance until 70 mm and increases rapidly to until detector distance of 120 mm after which it stays almost constant. For source distances of 230 mm and 300 mm, the CNR also drops for detector distance of 70 mm and increases beyond that with an exception at detector distance of 120 mm for source distance of 300 mm.

In fig:colallrey, images A and B are the images of the collagen samples in air, C and D are of the collagen samples in ethanol, and E and F are of the collagen samples in water. A, C, and E are the absorption images and B, D, and F are the edge-enhanced phase images. In the edge-enhanced phase images of the collagen samples in air, the edges of the pure collagen on the top are clearly visible whereas in the absorption image the edges fade out and no clear edge is visible. In the cross-sectional slices of the collagen samples in ethanol, the edge-enhanced phase image appears overall clearer and the PLA fibers in the bottom are more pronounced. The biggest difference is seen in the images of the collagen samples in water. In the absorption image, no clear details of the collagen samples can be seen, only the divider between the samples is visible. In the edge-enhanced phase image, the collagen sample with PLA is on top and the PLA fibers are clearly visible. The pure collagen sample is not recognizable in either image.

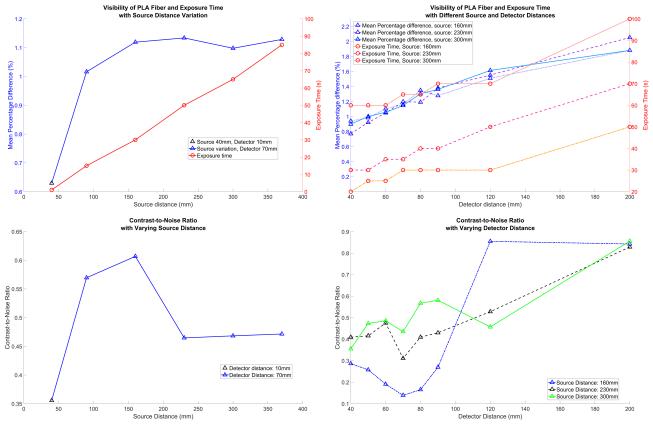

Fig. 2. Results of the fiber visibility analysis along with exposure time for the source variation measurements in the upper left graph and the results of the CNR calculations in the upper right graph. Fiber visibility of the detector variation measurements for three source distances along with exposure times in the bottom left graph and the CNR calculations for the detector variation measurements for three source distances in the bottom right graph. In both of the left side graphs, the black triangles at source distance of 40 mm are the absorption mode images.

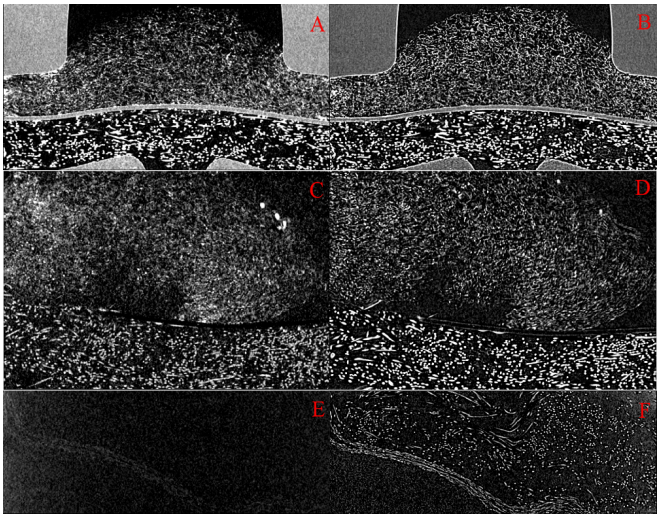

Fig. 3. Cross-sectional slices of the collagen samples in air (A & B), in ethanol (C & D), and in water (E & F). Images A, C, and E are obtained using conventional absorption imaging settings, while images B, D, and F are obtained using edge-enhancing phase imaging settings. Pure collagen samples are placed on top of the collagen+PLA samples in A, B, C, and D while in E and F the pure collagen sample is underneath the collagen+PLA sample.

IV. DISCUSSION

Due to the various factors affecting the amount of phase contrast visible, it was necessary to optimize the source and

detector distances for optimal contrast enhancement in low density sample applications.

For the detector distance measurements, the expectation was that the fiber visibility would increase to some distance with increasing detector distance but beyond this, the visibility would drop due to increasing noise and backscatter. Contrary to this, the results show that the visibility in fact increases with increasing detector distance. As the voxel size decreases with increasing detector distance, it could explain the increase in visibility of the PLA fiber. Overall, the change in visibility between different source distances is relatively small as can be seen from the upper right graph in fig:allcnrvisi.

As the Xradia MicroXCT-400 cannot separate phase and absorption information, it provides an edge-enhancement effect on low density samples. Due to this, the optimal settings for low density samples on this particular μCT device is obtained when the effect of edge-enhancement is clearly visible and absorption information of the sample is still obtained without a significant increase in noise. The first analysis of the fiber visibility was selected to evaluate the visibility of the phase effect at the fiber-ethanol interface. This was used to select the settings for the tomographic acquisition. The second analysis of CNR was selected to evaluate the contrast of the fiber with respect to the background. As this was performed after the tomographic acquisition, the combination of the result was not used to select the optimal acquisition settings. Additionally, the CNR analysis was only performed on the images obtained of the 107 μm PLA fibers, the results only represent those images and cannot necessarily be generalized for all fiber sizes.

The study could be continued by obtaining a tomographic acquisitions using a source distance of 160 mm and a detector distance of 120 mm. Furthermore, these optimization results can be used as a good starting point in upcoming image acquisitions if an edge-enhancing phase effect is required to enhance visibility of low density samples.

V. CONCLUSIONS

The phase imaging possibility on the Xradia MicroXCT-400 provides a technique to enhance the visibility of low density samples where neighboring structures have matching or similar densities. This requires an increase in exposure time but has the capability of revealing structures that are not visible otherwise.

CONFLICT OF INTEREST

The authors declare that they have no conflict of interest.

ACKNOWLEDGMENT

The authors aknowledge Minna Kellomäki's Biomaterials and Tissue Engineering Group for providing the PLA fibers used in the optimization process as well as Anne-Marie Haaparanta for providing the collagen samples used to test the optimization parameters.

REFERENCES

[1] Metscher B (2009) MicroCT for developmental biology: A versatile tool for high-contrast 3D imaging at histological resolutions. *Dev Dynam* 238(3): 632-640

[2] Mizutani R and Suzuki Y (2102) X-ray microtomography in biology. *Micron* 43(2-3): 104-115

[3] Hannula M, Haaparanta A-M, Tamminen I, Aula A, Kellomäki M, Hyttinen J (2016) X-ray Microtomography of Collagen and Polylactide Samples in Liquids, IFMBE Proc. vol. 57, XIV MEDICON, Paphos, Cyprus, 2016, pp 420-424

[4] Berndt S, Konz I, Colin D, Germain S, Pittet-Cuénod B, Klok H, Modarressi A (2017) Microcomputed Tomography Technique for In Vivo Three-Dimensional Fat Tissue Volume Evaluation After Polymer Injection. *Tissue Eng Pt C-Meth* 23:964-970

[5] du Plessis A, le Roux S, Guelpa A (2016) Comparison of medical and industrial X-ray computed tomography for non-destructive testing. *Nondestruct Test Eval* 6:17-25

[6] 5. Ferreira C, Lopes R, dos Santos T, Oliveira D, Martins F, Pereira G (2018) Non-destructive inspection of laminated pipe joints in polymeric composite material reinforced by fiberglass. *Nucl Instrum Meth A* (in press)

[7] Bushberg J (2002) The Essential Physics of Medical Imaging. Lippincott Williams & Wilkins, Philadelphia

[8] Arhatari B, Hannah K, Balaur E and Peele A (2008) Phase imaging using a polychromatic x-ray laboratory source. *Opt Express* 16(24): 19950-19956

[9] Chen G, Zambelli J, Bevins N, Qi Z, and Li K (2010) X-ray Phase Sensitive Imaging Methods: Basic Physical Principles and Potential Medical Applications. *Curr Med Imaging Rev* 6(2): 90-99

[10] Wu X and Liu H (2003) A general theoretical formalism for X-ray phase contrast imaging. *J X-Ray Sci Technol* 11: 33-42

[11] Snigirev A, Snigireva I, Kohn V, Kuznetsov S and Schelokov I (1995) On the possibilities of X-ray phase contrast microimaging by coherent high-energy synchrotron radiation. *Rev Sci Instrum* 66(12): 5486-5492

[12] Wilkins S, Gureyev T, Gao D, Pogany A and Stevenson A Phase-contrast imaging using polychromatic hard X-rays. *Nature* 384(6607): 335-338

[13] Pogany A, Gao D and Wilkins S (1997) Contrast and resolution in imaging with a microfocus x-ray source. *Rev Sci Instrum* 68(7): 2774-2782

[14] Reunamo A (2019) Augmenting Soft-Tissue Contrast Using Phase-Contrast Techniques in Micro-Computed Tomography Imaging. Master's thesis, University of Eastern Finland (to be published)

[15] Kroon M (2017) A Comparative In Vitro Study of Cell Growth on Textile Scaffolds for Tissue Engineering Applications. Master's thesis, Tampere University of Technology

[16] Schindelin J, Arganda-Carreras I, and Frise E (2012) Fiji: an open-source platform for biological-image analysis. *Nat Methods* 9(7): 676-682

[17] Haaparanta A-M, Koivurinta J, Hämäläinen E-R, and Kellomäki M (2008) The effect of cross-linking time on a porous freeze-dried collagen scaffold using 1-ethyl-3-(3-dimethylaminopropyl)carbodiimide as a cross-linker. *J Appl Biomater Biom* 6(2):89-94

Author: Aino Reunamo
Institute: Tampere University
Street: Arvo Ylpön katu 34
City: Tampere
Country: Finland
Email: aino.reunamo@tuni.fi